SUPPORTING MATERIALS & METHODS

Kinesin-1 Motors Can Circumvent Permanent Roadblocks by Side-Shifting to Neighboring Protofilaments

René Schneider, Till Korten, Wilhelm J. Walter, and Stefan Diez

---

SUPPORTING MATERIAL

A. Roadblocks are immobile and irreversibly bound on microtubules

To investigate the binding of roadblocks with microtubules (MTs) we used the GFP-labeled version of the roadblocks (see Materials & Methods). To decorate the MTs with roadblocks we incubated the channel of the flow cell with 0.2 - 15 nM roadblock and performed objective-type TIRF microscopy (Supporting Fig. S1A). We found that individual roadblocks bound immobile and irreversibly to MTs (Supporting Fig. S1B,C). When comparing the integrated intensity of roadblocks bound along the MTs before and after a waiting period of 20 minutes, no significant reduction in the roadblock density was observed (Supporting Fig. S1C, left pair of columns). The density reduced by approximately 400 counts per µm which, using the average fluorescence signal of individual roadblocks of approximately 650 counts per µm, converts into an upper limit for the off-rate k_{off} of 0.001 s^{-1}. Thus, in absence of roadblocks in solution, the dissociation of roadblocks was slow (approximately one roadblock per µm detached within the 20-minute waiting period). The off-rate remained unaffected even when ‘active’ motors were allowed to interact for 20 minutes (Supporting Fig. S1C, middle and right pair of columns). Thus, the kinesin-1 motors were not able to remove roadblocks from the MTs.

B. Simulation of Poisson steppers on roadblock-decorated protofilaments

Poisson steppers were simulated to land uniformly on free stretches along a protofilament (see Supporting Fig. S3A,B). For each stepper, a long series of 8 nm steps (N_{steps} >> 1000) was generated with random, exponentially distributed times between the steps (values chosen from an exponential probability distribution with a mean of 0.01 s (= 8 nm ÷ 800 nm/s). Subsequently, the dwell time of the stepper was chosen from another exponential probability distribution with a mean of 1.0 s. The series of steps was then shortened to match the obtained dwell time. This procedure yielded trajectories, which did not take roadblock encounters into consideration (see Supporting Fig. S3C). The trajectories were then projected onto the protofilament, starting from a random landing position and cropped in case the trajectory extended over the protofilament end. Roadblock encounters were considered by testing if randomly distributed roadblocks were located along the trajectory. In this case, the trajectory was cropped at the position of the first roadblock (see Supporting Fig. S3D). From this point, three cases were considered, which gave rise to the scenarios (i) to (iii) in the main text (see Fig. 2D): For the 'no waiting, no circumvention' scenario (Fig. 2Diii), no further post-procession of the trajectories was performed. Thus trajectories ended upon encounter of a roadblock (see Supporting Fig. S3D, red line). For the 'waiting, no circumvention' scenario (Fig. 2Dii), we extended the dwell time of the motor by adding a randomly chosen waiting time (chosen from an exponential probability distribution with a mean of 0.4 s). After expiration of the waiting time, the motor trajectory ended (see Supporting Fig. S3D, orange line). For the 'waiting and circumvention' scenario (Fig. 2Di), we extended both, the dwell time (according to the 'waiting, no circumvention' scenario) and the run length by considering another series of steps after the roadblock was circumvented (i.e. after expiration of the waiting time). If a roadblock was circumvented or not was decided by picking a random number between 0 and 100. We used a circumvention probability of 30 %, i.e. circumvention was allowed when the random number was found between 0 and 30. The trajectory after roadblock circumvention was affixed to the end point of the previous trajectory (see Supporting Fig. S3D, green line). Multiple roadblock encounters were considered by allowing several cycles of dwell time and run length 'post-processing'. Trajectories ended when (i) the random number was larger than the input circumvention probability (i.e. no circumvention but waiting), (ii) when the trajectory of the motor ended before reaching the next roadblock, or (iii) when the trajectory of the motor extended over the protofilament end. We choose a total protofilament length of 1000 µm to reduce the likelihood of end-effects. The influence of the imaging process was considered by (i)

averaging the position of the steppers in 100 ms intervals (given by the exposure time) and by (ii) adding a localization error of 30 nm (see Supporting Fig. S3E, values for localization precision from (18)).

The fact that the 'no waiting, no circumvention' scenario produced mean run lengths slightly exceeding the predominant mean roadblock spacing (see Fig. 2B) can be explained by our restriction to minimum trajectory durations of 4 frames (see Material & Methods). This causes a bias towards long dwell times, which becomes severe in the 'no waiting, no circumvention' scenario because motors detach immediately upon roadblock encounter. This means that out of our distribution of motors, only those that walk in between roadblocks which are significantly further apart than the mean roadblock spacing can generate trajectory durations of ≥ 4 frames. In fact, at the highest mean roadblock spacing of 94 nm, out of the 1000 simulated motors, only 49 motor trajectories were found that showed durations of ≥ 4 frames. Furthermore, motors that, due to the random nature of the Poisson stepper, have a velocity slower than the mean motor velocity are favored because they are more likely to last for >4 frames (hence the small decrease of mean velocities for the red line in Fig. 2A).

C. Determining the roadblock spacing along individual protofilaments

Four assumptions were made to convert roadblock density along the MTs into a density along an individual protofilament: *Firstly*, only the 'upper' half of the MTs, i.e. the protofilaments facing toward solution, were accessible for motors. This assumption is reasonable because the MTs were immobilized to the glass substrate using antibodies ($5-10$ nm in size), which are relatively small compared to the motors (two 5 nm heads + 30 nm tails). *Secondly*, the calibration curve obtained for GFP-labeled roadblocks also holds true for unlabeled roadblocks, i.e. both version of the roadblock have similar affinity for the MT. This was confirmed by comparing the decrease of the mean velocity in presence of labeled and unlabeled roadblock. In both cases, the mean velocity decreased to 1/e with similar mono-exponential decay constants (GFP-labeled roadblocks: 3.4 ± 0.5 nM, unlabeled roadblocks: 3.1 ± 0.5 nM, mean ± fit error, $N = 6$). *Thirdly*, a low constant amount of intrinsic obstacles, e.g. formed by the antibodies, defective tubulin or tubulin-copurified MAPs, is present on the MTs even in the absence of added roadblocks (compare Supporting Fig. S2, top left graph, where 25 % of the motors showed slow velocities caused by temporary waiting). We ruled out that 'dead' motors were responsible for this effect by measuring the dwell time of the slow motor population (all motors slower than 200 nm/s) and

compared it to the dwell time of the fast motor population (all motors faster than 200 nm/s). We found that the dwell time of the slow motors was in a similar range as the dwell time of the fast motors ('slow': 1.19 ± 0.24 s, mean ± sd, $N = 65$ molecules, fast: 0.89 ± 0.06 s, $N = 273$) however, still much shorter than the predominant bleaching time of 5.8 ± 0.9 s (mean ± sd, $N = 3$ movies with ≥ 75 molecules each). If 'dead' motors were present one would expect the dwell time of the slow motor population to be significantly longer, close to the bleaching time. *Fourthly*, we assumed that all GFP-labeled roadblocks were fluorescent, i.e. the number of bleached, mis-folded or otherwise non-functional GFP-labels was low. This assumption may lead to a slight underestimation of the roadblock spacing.

D. Proofs for single-molecule conditions

Single-molecule conditions were guaranteed by optimizing the incubation stoichiometry of antibody-conjugated AuNPs and motor molecules and by comparing the motility parameters of the AuNP-loaded motors to unloaded (GFP-labeled) motors in absence and presence of roadblocks.

Incubation stoichiometry: The number of motors bound to beads follows Poisson statistics (35). Thus, in the ideal case that all beads are bound to a motor, a 10:1 ratio of beads to motors provides a 95 % confidence that bead-movement was caused by the action of an individual motor. Using this argument as a starting point we tested several incubation ratios of antiGFP-conjugated AuNPs to GFP-labeled motors. Moving AuNPs were found only for incubation ratios of 5:1 and lower. Under these conditions, we observed a 100-fold higher landing rate for unbound motors compared to AuNP-loaded motors. Thus, most motors were unloaded, i.e. had no AuNP bound to it. Ratios of up to 1:1 still only yielded a 50-fold lower landing rate of AuNP-loaded motors compared to unloaded motors. We reason that the large number of unbound motors originates from the nanomolar-affinity of the GFP-antibody for the GFP-antigen on the tails of kinesin-1. Since concentrations in the nanomolar range were used during incubation of AuNPs and motors, only a small fraction of AuNPs found a GFP-labeled motor. Under these conditions it was estimated (based on the assumption that the on-rate of AuNP-loaded and unloaded motors to the MT scales with the diffusion constant D ($D_{\mathrm{AuNP}} \cong 10\ \mu m^2/s$ estimated from Einstein relation, $D_{\mathrm{GFP}} \cong 70\ \mu m^2/s$ from (36), both in water at 20° C), that only 10 % of the motors were bound to a AuNP. This leads to a AuNP-to-motor ratio of 10:1, providing a 95 % confidence that AuNP transport was due to the action of individual motors.

Motility parameters of AuNP-loaded motors: A second argument for single-molecule conditions was obtained by comparing the mean velocity, mean run length, and mean dwell time of AuNP-loaded to unloaded motors. It was shown that the association of more than one motor to either quantum dots or DNA origami scaffolds caused the mean dwell time and the mean run length to drastically increase about 3-fold (37-39). Evidence for single-molecule movement is therefore provided, if AuNP-loaded motors show similar motility parameters compared to unloaded motors. This comparison was complicated by the GFP-label being subject to photobleaching, whereas the AuNPs can be considered as optically stable. Therefore, we applied a bleaching-correction of the dwell time and run length of GFP-labeled motors (22) (Materials & Methods). Using the parabolic prism-type TIR setup, the bleaching time of GFP-labeled motors was determined to 2.5 ± 1.0 s (mean ± sd, N = 3 movies).

In absence of roadblocks, AuNP-loaded motors showed similar mean velocities compared to unloaded motors (Supporting Fig. S7A and Supporting Table S2). Therefore, we concluded that the AuNP did not provide enough drag force to cause a noticeable slow-down of the motors. Furthermore, we found that the run lengths and dwell times of AuNP-loaded and unloaded motors were not significantly different (Supporting Fig. S7B,C and Supporting Table S2). In particular, AuNP-loaded motors showed only ~ 1.2-fold larger dwell times which is less than the 3-fold enhancement expected for multi-motor transport (38, 39). Larger dwell times of up to five seconds were only observed when incubating antibody-conjugated AuNPs with a 10-fold excess of motors. Only then, AuNPs were transported along the complete length of the MT often only detaching when reaching the end of the MT.

In presence of roadblocks, AuNP-loaded motors showed a similar deterioration of the motility parameters compared to the GFP-labeled motors. The mean velocity of AuNP-loaded motors was slightly higher compared to the unloaded motors. This increase originated from the fact that some non-moving AuNPs were excluded from the evaluation, when their attachment or detachment was not recorded within the movie stream (see Materials & Methods). The deterioration of the run length and dwell time were in agreement with the previously obtained results for GFP-labeled motors (compare with Fig. 2B,C in the main text). Thus it is concluded, that AuNP-loaded and unloaded motors showed a similar deterioration of motility parameters. Taken together, these results suggest that AuNPs were majorly transported by individual motors.

E. Geometrical considerations on AuNP-loaded motors walking along MTs

The 40 nm AuNP resembled a relatively large label compared to the size of the motor domains (~ 5 nm) and the MT diameter (25 nm). Thus, knowledge about the three-dimensional arrangement of the AuNP-loaded motors to the surface-immobilized MTs is of particular interest for this study.

(i) Motor-to-AuNP linker: We gained insight into the length of the motor-to-AuNP linker by investigating a motor trajectory, which showed several successive transverse shifts, thereby transitioning from a protofilament on the far left to a protofilament on the far right side of the MT (Supporting Fig. S10). The total shifted transverse distance for that trajectory was determined to approximately 130 nm (= 13.0 nm + 33.3 nm + 79.8 nm). Thus, the tail-bound AuNP could reach radially outward by approximately 65 nm from the MT centerline. Subtracting the radius of the MT (12.5 nm) and the AuNP (20 nm) leaves approximately 32.5 nm for the motor-to-AuNP linker. The linker, consisting of streptavidin, biotinylated GFP-antibody, EGFP at the motor tail and the tail themselves, was estimated to a total length of about 30 nm previously (18). The finding of a 32.5 nm linker is therefore evidence for the motor tail being in a rather stretched configuration.

(ii) Number of accessible protofilaments: Moreover, this trajectory allowed estimating the number of protofilaments available for AuNP-loaded motors. Provided that the motor tails extended radially outward from the MT, only the top half of the MT (protofilaments facing toward solution) are accessible for AuNP-loaded motors. The protofilaments positioned on the bottom half of the MT are only accessible if the motor tail is allowed to bend so that the motor can reach underneath the MT while transporting the AuNP. We observed that AuNP-loaded motors showed approximately five distinct fluctuation regimes in Supporting Fig. S10. This observation suggested that the AuNP – being flexibly tethered to the motor tail – exhibits restricted diffusion when the motor is located on a lateral protofilament, while it can freely explore the volume around the MT when the motor is located on the topmost protofilaments. We could use these distinct fluctuation regimes to identify the number of available protofilaments for this event ($N_{\text{protofilaments}} = 5$). The different absolute sizes of the oppositely oriented third and fourth transverse shift (−79.8 nm and +31.7 nm, respectively) in Supporting Fig. S10 indicated that transverse shifts also occurred between one and the second-next protofilament. However, these shifts were rare (< 10 % of the total transverse shifts). Thus we conclude that transverse shifts majorly occur between neighboring protofilaments.

(iii) Amplification of transverse shifts: 90% of the transverse shifts showed amplitudes smaller than ± 40 nm (Fig. 3D), which is consistent with our geometrical expectations. Assuming that a AuNP-loaded motor extends radially outward from the MT centerline, the largest side-shifts are expected when the motor shifts between the two topmost protofilaments (see inset in Fig. 3A). The amplitude of these transverse shifts can be calculated by $s = 2 \sin(\pi/13) \times L$, where L is the distance between the center of the AuNP and the center of the MT. Both, geometrical considerations and experimental data (Supporting Fig. S10) estimate this distance to be about 65 nm, leading to maximal amplitudes of about 31 nm in close agreement with the largest detected transverse shift in the histogram (compare Fig. 3D). It is not surprising however, that most of the transverse shifts showed smaller amplitudes of approximately 10 nm and below. This is because the amplitude of a transverse shift depends on the location of the protofilaments between which the shift occurs. Thus, transitions between protofilaments on the side of the MT produce smaller transverse shifts than transitions between protofilaments on top of the MT. The smallest transverse shifts being detected were often insignificant and resembled a sharp peak located between minus 4 nm and plus 4 nm (Supporting Fig. S11), in agreement with previously published localization errors for AuNP-loaded motors (18). The remaining 10 % of the transverse shifts with amplitudes larger than ± 40 nm (maximally up to 80 nm) are attributed to transitions between further distanced protofilaments (e.g. between one and the second-next protofilament).

(iv) Transverse fluctuation: We note, that the position of the motor on the MT can also be inferred from the transverse fluctuations. For example, the trajectory in Fig. 3C shows two successive transverse shifts from a protofilament on the side of the MT toward the MT centerline. Each transverse shift is coupled to a change in the transverse fluctuation – the largest fluctuations were observed when the AuNP-loaded motors moved on topmost protofilaments (Supporting Fig. S10).

(v) Motors switching protofilaments without prior waiting show similar transverse shifts: Interestingly, we found that 25 % of AuNP-loaded motors moving uniformly also showed transverse shifts without showing a prior waiting phase (also see Supporting Fig. S8). The corresponding transverse shifts were similar to the transverse shifts of pausing motors (see Supporting Fig. S11B).

SUPPORTING FIGURES

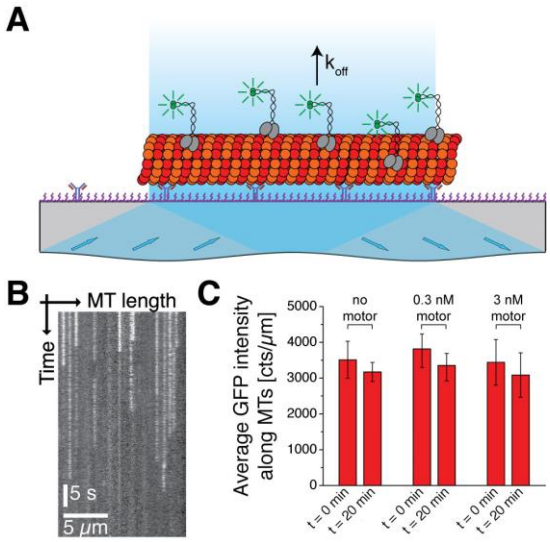

Fig. S1 | Roadblock dissociation from surface-immobilized MTs.
(A) TIRF microscopy assay to measure the dissociation rate (off-rate k_{off}) of GFP-labeled roadblocks from MTs. (B) Kymograph of individual roadblocks bound along a MT. The roadblocks were static (velocity of 0.3 ± 1.2 nm/s, mean ± sd, $N = 34$ molecules) and bleached with a time constant of 16.1 ± 0.8 s (mean ± fit error). (C) Integrated roadblock intensity along MTs at start (0 min) and after 0 nM (left), 0.3 nM (middle), and 3 nM (right) GFP-labeled motors were present for 20 min. Intensity was measured after washing the channel with fresh imaging solution, i.e. in absence of active GFP-labeled motors.

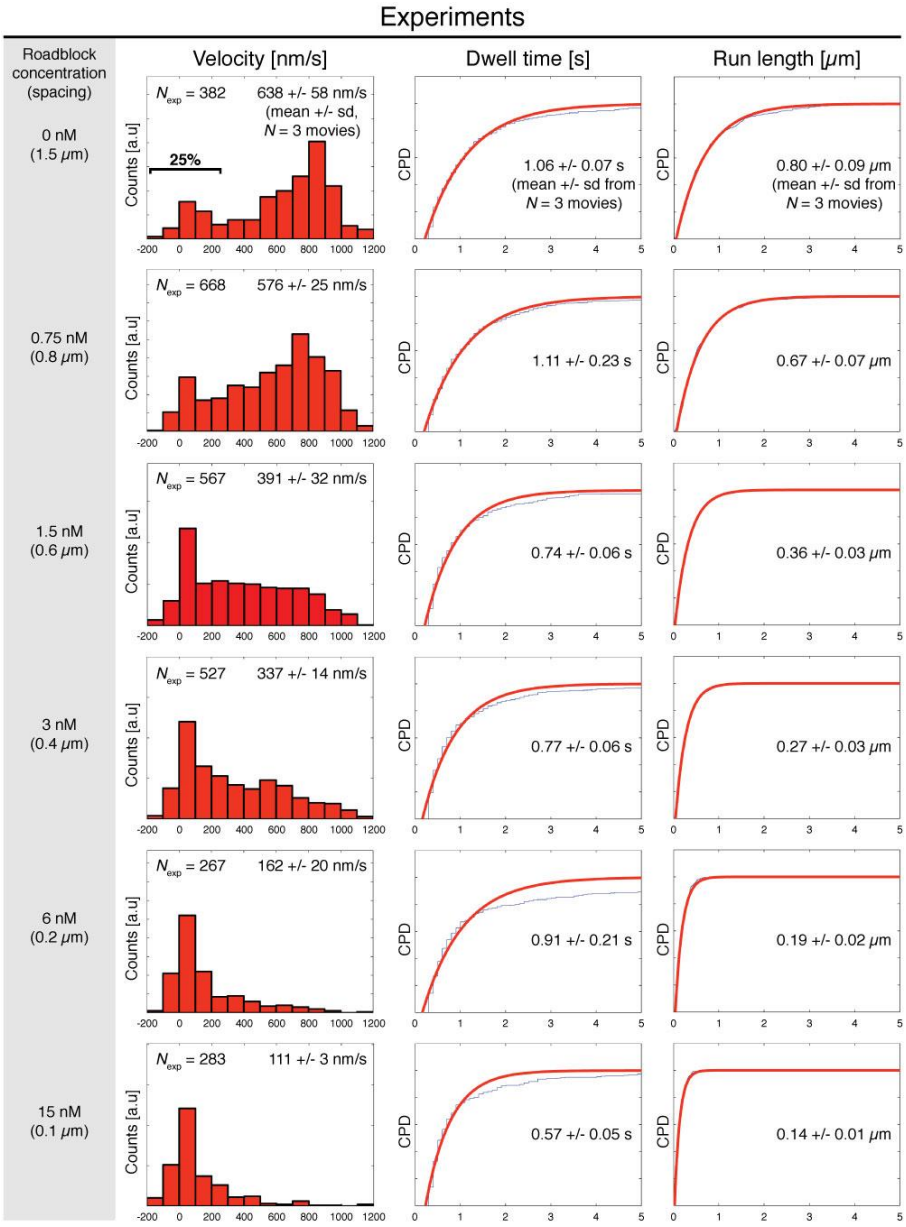

Fig. S2 | Determination of the mean velocity, mean run length, mean dwell time, and mean waiting time for each roadblock condition

Histograms of the velocities (1st column) and cumulative probability distributions (CPDs) of dwell times (2nd column), and run lengths (3rd column) of individual motors from one representative movie at each roadblock condition (roadblock concentrations and the corresponding spacings are given in the grey column). CPDs were fitted with a mono-exponential function (red solid lines) to yield the ensemble dwell time, and run length, respectively. The mean and standard deviations for each motility parameter were calculated by averaging over three independent measurements of the ensemble velocity, dwell time, and run length at each roadblock condition.

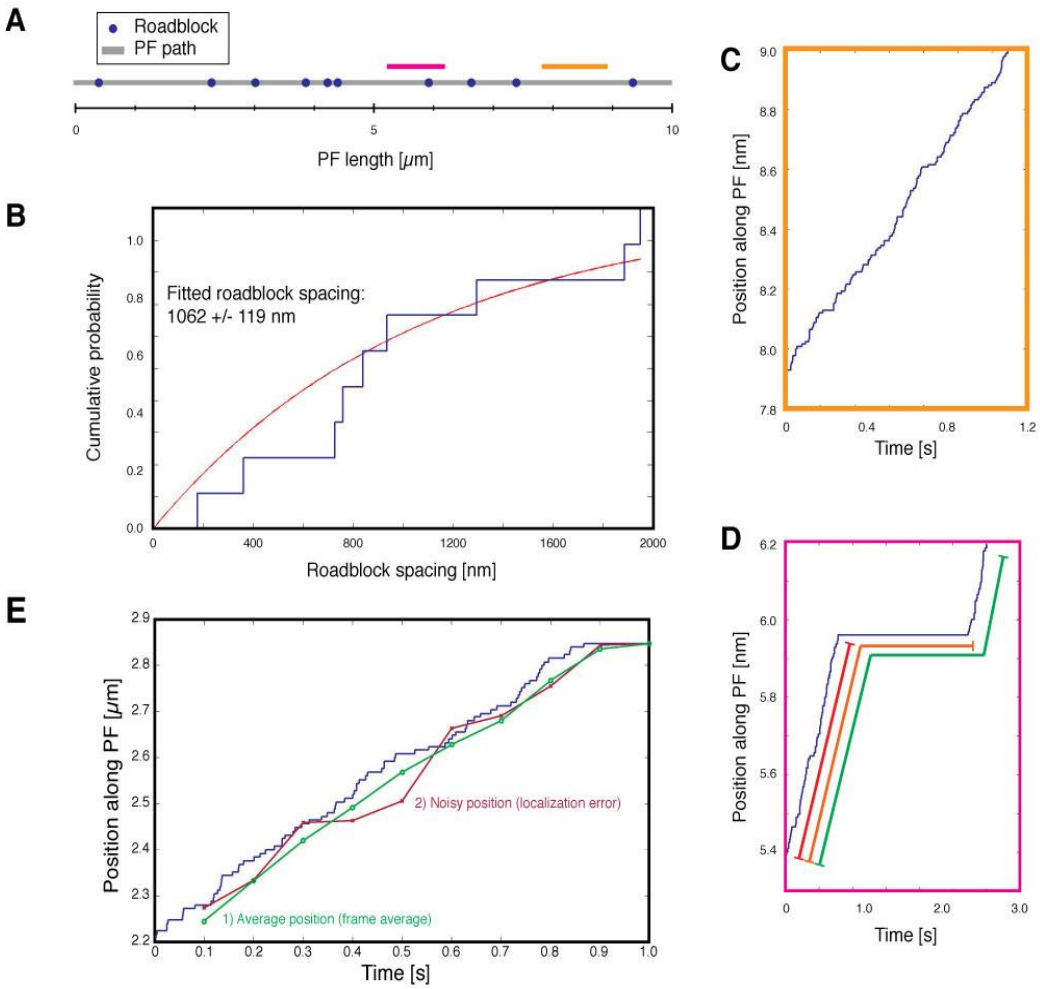

Fig. S3 | Simulated motor trajectories in the presence of roadblocks
(A) Exemplary protofilament (PF, 10 µm length, grey line) decorated randomly with 10 roadblocks (blue dots). Poisson steppers were allowed to land uniformly on the protofilament. Two example events were highlighted: One motor performed an unimpeded walk along the protofilament (orange line, see C), the other motor encountered a roadblock, waited, and continued the run after roadblock circumvention (magenta line, see D). (B) CPD of the roadblock spacings (blue line) was used as control of the pre-defined roadblock spacing (here: 1000 nm). The average roadblock spacing was determined by fitting an exponential function to the CPD (red line, 1062 ± 119 nm, mean ± fit error, N = 9 roadblock spacings). (C) Example trace from (A) of an unimpeded motor. (D) Example trace from (A) of a motor circumventing a roadblock after a waiting phase. In scenario (i) ('waiting and circumvention') the trajectory was extended in 30 % and ended in 70 % of the encounters, respectively (green line). In scenario (ii) ('waiting and no circumvention') a waiting phase was incorporated into the trajectory (orange line). In scenario (iii) ('no waiting, no circumvention') the trajectory ended when a roadblock was encountered (red line). (E) Temporal averaging (green circles) and spatial noising (red crosses) were added to the simulated trajectories to mimic the imaging process.

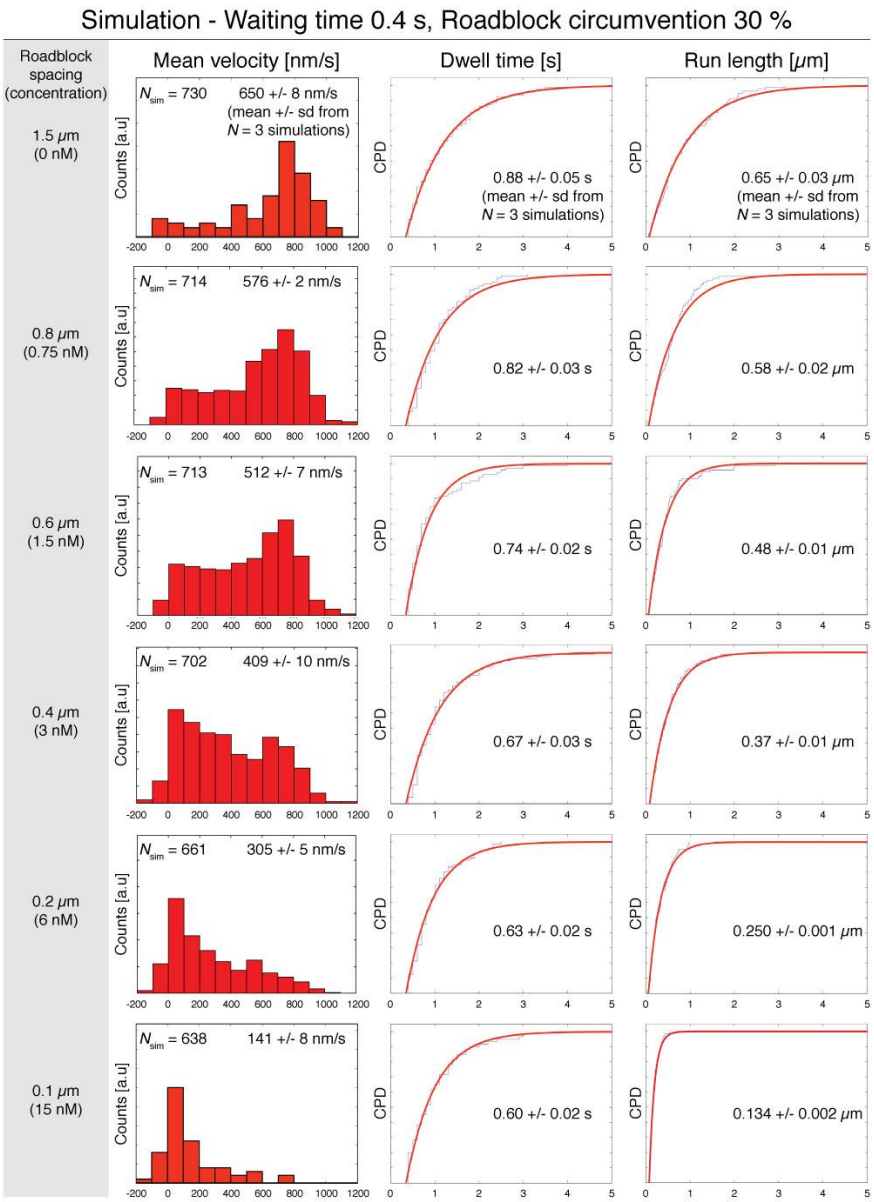

Fig. S4 | Simulated motility parameters at each roadblock spacing
Histograms of velocities (1st column) and CPDs of dwell times (2nd column) and run lengths (3rd column) of individual simulated motors ($N = 1000$ molecules per simulation, 3 simulation runs per condition, roadblock spacings and corresponding concentrations are given in the grey column). CPDs were fitted with a mono-exponential function (red solid line) to yield the ensemble dwell time and run length, respectively. Roadblock spacings were converted into roadblock concentrations using the calibration curve from Fig. S5. The means and standard deviations for each motility parameter were calculated by averaging over three independent measurements of the ensemble velocity, dwell time, and run length.

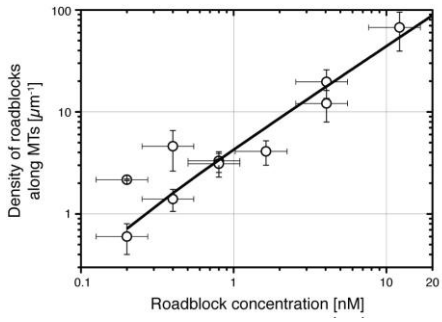

Fig. S5 | Calibration curve for roadblocks binding to MTs.
The density of roadblocks bound along surface-immobilized MTs being incubated for 1 minute with varying roadblock concentrations (open circles, density error bars are standard deviations, concentration error bars were estimated from the error in protein concentration). In the measured range, the relation was found to be linear (black solid line; weighted linear fit).

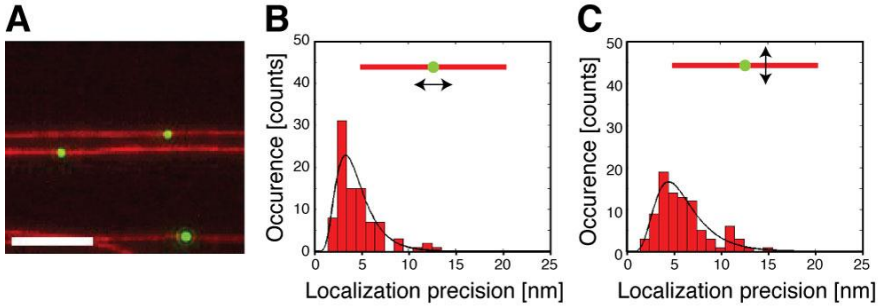

Fig. S6 | Localization precision of AuNP-loaded roadblocks.
(A) Color-combined image of surface-immobilized rhodamine-labeled MTs (red) decorated with AuNP-loaded roadblocks (green, GFP-antibody conjugated AuNPs coupled to the GFP-labeled tails of roadblocks). Scale bar: 5 µm. (B) Histogram of localization precision parallel to the MT axis. A lognormal fit yielded an average localization precision of 4.5 ± 2.0 nm (mean ± sd, N = 90 AuNPs). (C) Histogram of localization precision perpendicular to the MT axis. Lognormal fitting yielded an average localization precision of 6.1 ± 2.8 nm.

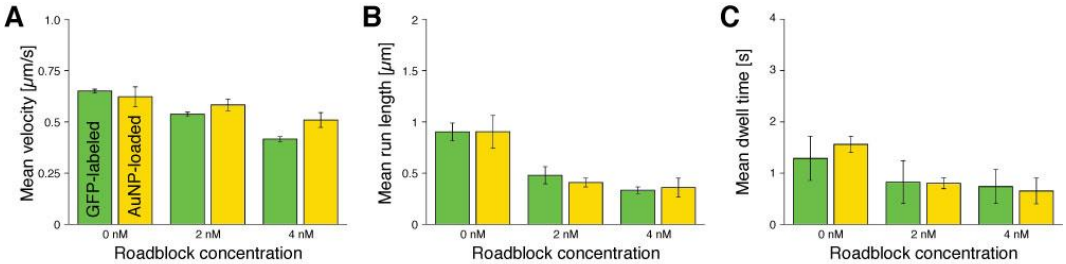

Fig. S7 | Motility parameters for GFP-labeled (unloaded) and AuNP-loaded motors at 0 nM, 2 nM, and 4 nM roadblocks.
(A) The mean velocities of unloaded motors (green bars, mean ± sem) were not statistically different from the mean velocities of AuNP-loaded motors (yellow bars) for all three roadblock conditions. The mean run length (B) and the mean dwell time (C) of AuNP-loaded motors (mean ± sd) overlapped with the bleaching-corrected mean run length and mean dwell time, respectively, of unloaded motors at all conditions.

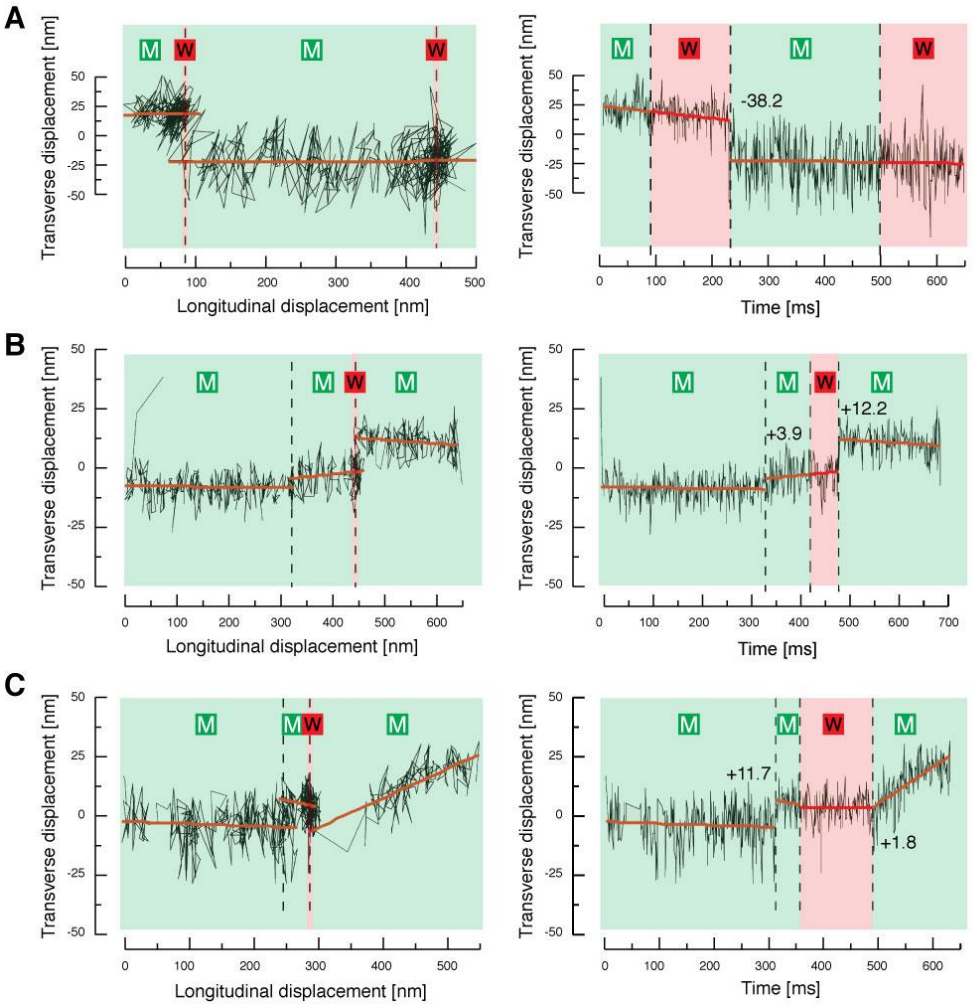

Fig. S8 | Typical trajectories of pausing motors at 2 nM roadblock
Transverse displacement versus longitudinal displacement (left) and versus time (right). Dashed lines depict transitions between moving (M) and waiting (W) phases. The size of the transverse shift is given at each transition. A negative shift depicts movements toward the right. (A) A motor showing a large transverse shift: −38.2 nm toward the right followed by continuation of the run. (B) A motor showing a transverse shift without a prior waiting phase: sudden +3.9 nm shift toward the left without a detectable waiting phase followed by roadblock encounter and circumvention by a transverse shift of +12.2 nm toward the left after a waiting phase. (C) A motor showing a large forward shift: +11.7 nm shift toward the left without a prior waiting phase followed by a roadblock encounter and a waiting phase. Circumvention is achieved by a +150 nm forward shift, presumably onto the same protofilament (transverse shift of only +1.8 nm).

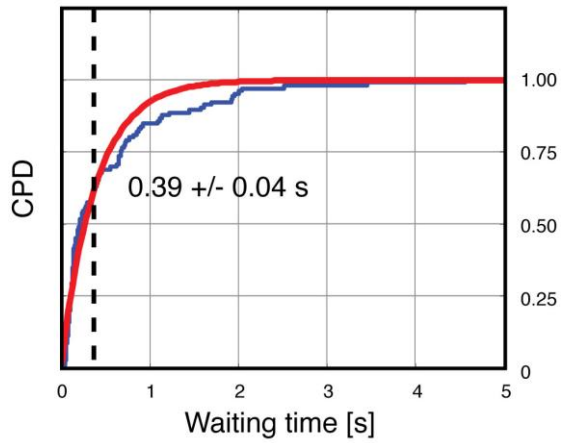

Fig. S9 | Waiting time of AuNP-loaded pausing motors
Cumulative probability plot of the waiting times of 106 pausing motors (blue line). Mono-exponential fitting (red line) yielded a mean waiting time of 0.39 ± 0.04 s (indicated by dashed black line, mean ± fit error).

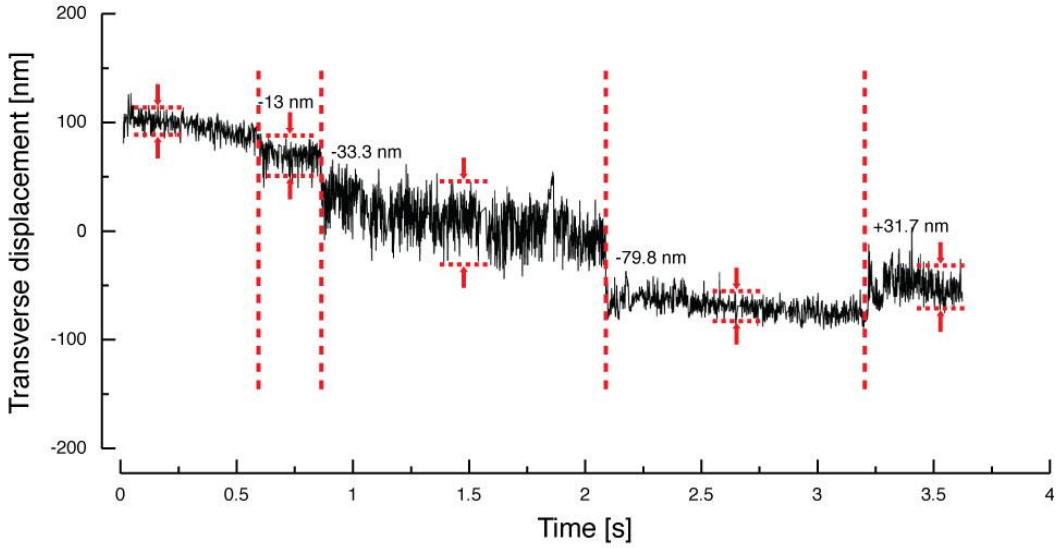

Fig. S10 | Exemplary trajectory to estimate the extension of the motor-to-AuNP linker and the number of accessible protofilaments.
A motor trajectory showing multiple transverse shifts from the far left to the far right protofilament (shifts indicated by dotted lines, the size of the shift is given at each transition). More than three side-shifts were observed in less than 2 % of all trajectories. Each transverse shift was correlated with a change in the amplitude of the transverse fluctuation – from small, when the AuNP-loaded motor is on a protofilament on the side, to large, when the motor is on a topmost protofilament. We detected a pause only for the last of the four side-shifts.

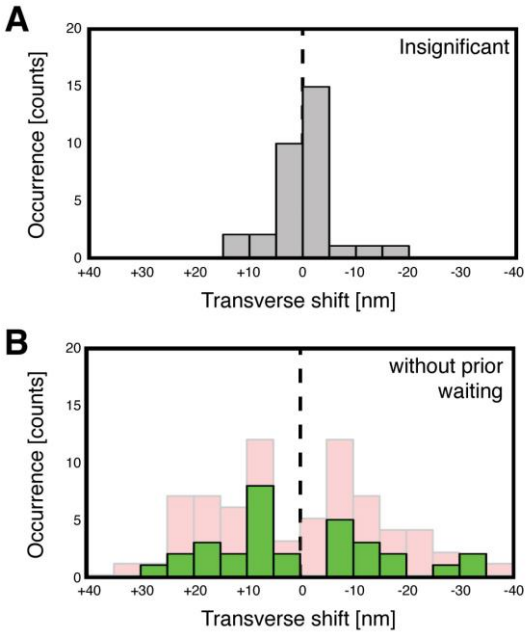

Fig. S11 | Histograms of insignificant shifts from pausing motors and significant shifts from motors showing no prior waiting phase

(A) Insignificant transverse shifts (grey bars, $N = 30$ motors) were separated from the transverse shift histogram of the 106 total pausing motors (see Fig. 3D). (B) Motors, which showed side-shifts without prior waiting (green bars, $N = 37$ side-shifts), resembled a similar distribution of transverse shifts compared to pausing motors (underlayed in faint red).

SUPPORTING TABLES

Table S1 | Classification of the trajectories of GFP-labeled motors for each roadblock condition[a]

Roadblock concentration [nM]	N_{motors}	Moving [%]	Stopping [%]	Starting [%]	Pausing [%]	Waiting [%]	Circumvention probability [%][b]
0	382	82%	8%	2%	4%	4%	33%
0.75	668	75%	9%	3%	5%	8%	32%
1.5	567	41%	18%	6%	8%	27%	24%
3	527	32%	18%	8%	9%	33%	25%
6	267	22%	18%	11%	8%	41%	24%
15	283	17%	21%	9%	8%	45%	20%
0[c]	910	72%	12%	2%	7%	7%	32%

[a] Classification of trajectories was performed on kymographs from at least three different MTs from three different movies at each roadblock condition.
[b] Circumvention probability calculated based on normalizing the number of starting and pausing motors to the total number of stopping, starting, pausing, and waiting motors.
[c] Control measurement at the end of the experiment

Table S2 | Motility parameters of GFP-labeled (unloaded) and AuNP-loaded motors at 0 nM, 2 nM, and 4 nM roadblock concentration.

Motility parameter	Unloaded motors	AuNP-loaded motors
Mean velocity [nm/s] (mean ± sem)	0 nM: 650 ± 9 (N = 805) 2 nM: 537 ± 10 (985) 4 nM: 416 ± 12 (649)	623 ± 48 (58) 583 ± 28 (112) 509 ± 37 (71)
Mean run length [µm] (mean ± sd)	0.90 ± 0.09 0.48 ± 0.08 0.33 ± 0.03	0.93 ± 0.16 0.41 ± 0.04 0.36 ± 0.09
Mean dwell time [s] (mean ± sd)	1.3 ± 0.4 0.82 ± 0.42 0.74 ± 0.33	1.5 ± 0.2 0.80 ± 0.11 0.65 ± 0.25

Table S3 | Classification of the trajectories of AuNP-loaded motors for each roadblock condition

Roadblock concentration [nM]	N_{motors}	Moving [%]	Stopping [%]	Starting [%]	Pausing [%]	Waiting [%]
0	63	49%	24%	5%	19%	3%
2	112	29%	27%	4%	29%	13%
4	71	14%	37%	8%	32%	8%

Table S4 | Event probabilities for AuNP-loaded motors during stepping and pausing[a]

	Event probability per 8-step [%][b]			Probability per waiting phase [%]		
	Detach	Wait	Significant transverse shift[c] without waiting	Detach after waiting	Continue after waiting	Significant transverse shift[c]
0 nM 8661 steps from 63 trajectories	0.73 ± 0.09 N_{detach} = 63	0.52 ± 0.08 N_{wait} = 45	0.18 ± 0.05 N_{side} = 16	46.7 ± 10.2 N_{detach} = 21	53.3 ± 10.9 $N_{continue}$ = 24	61 ± 16 14 events from 23 pausing phases
2 nM 8219 steps from 112 trajectories	1.36 ± 0.13 N_{detach} = 112	1.27 ± 0.12 N_{wait} = 104	0.16 ± 0.04 N_{side} = 13	48.1 ± 6.8 N_{detach} = 50	51.9 ± 7.1 $N_{continue}$ = 54	80 ± 13 41 events in 51 pausing phases
4 nM 6099 steps from 71 trajectories	1.16 ± 0.14 N_{detach} = 71	1.28 ± 0.14 N_{wait} = 78	0.13 ± 0.05 N_{side} = 8	51.3 ± 8.1 N_{detach} = 40	48.7 ± 7.9 $N_{continue}$ = 38	66 ± 14 21 events in 32 pausing phases

[a] Errors represent counting errors based on the total number of events.

[b] Probability based on the total number of 8-nm forward progressions (steps) which were calculated from the integrated run length of all considered events divided by 8 nm.

[c] A significant transverse shift was scored when the amplitude of the transverse shift was larger than the shift error.

SUPPORTING REFERENCES

35. Block, S.M., L.S.B. Goldstein, and B.J. Schnapp. 1990. Bead movement by single kinesin molecules studied with optical tweezers. Nature. 348: 348–352.
36. Howard, J. 2001. Mechanics of motor proteins and the cytoskeleton. 1st ed. Sinauer Associates Inc.
37. Seitz, A., and T. Surrey. 2006. Processive movement of single kinesins on crowded microtubules visualized using quantum dots. EMBO J. 25: 267–277.
38. Derr, N.D., B.S. Goodman, R. Jungmann, A.E. Leschziner, W.M. Shih, et al. 2012. Tug-of-war in motor protein ensembles revealed with a programmable DNA origami scaffold. Science. 338: 662–665.
39. Furuta, K., A. Furuta, Y.Y. Toyoshima, M. Amino, K. Oiwa, et al. 2013. Measuring collective transport by defined numbers of processive and nonprocessive kinesin motors. P. Natl. Acad. Sci. USA. 110: 501–506.